PHYSICAL REVIEW B **72**, 165409 (2005)

Field enhancement and gap-dependent resonance in a system of two opposing tip-to-tip Au nanotriangles

Arvind Sundaramurthy,* K. B. Crozier,† and G. S. Kino
E. L. Ginzton Laboratory, Stanford University, Stanford, California 94305, USA

D. P. Fromm, P. J. Schuck, and W. E. Moerner
Department of Chemistry, Stanford University, Stanford, California 94305, USA

(Received 12 May 2005; published 7 October 2005)

The enhancement of the electromagnetic field is described for nanoscale metallic "bowtie" antennas, consisting of two opposing tip-to-tip Au nanotriangles separated by a gap, through simulation and experiment. Currents, field distributions, and scattering efficiencies in the antennas at optical wavelengths are obtained from finite-difference time-domain (FDTD) simulations using realistic wavelength-dependent dielectric constants. The experimentally measured resonant wavelengths and intensity enhancements from individual bowtie antennas are in excellent agreement with the FDTD simulations. A simple physical model based on current distribution in the antennas is presented to understand the variation in resonant wavelength with gap and explain the basis for the field enhancement.

DOI: 10.1103/PhysRevB.72.165409 PACS number(s): 87.64.Xx

Metal nanoparticles have been studied extensively both theoretically and experimentally at optical and infrared wavelengths. The electric field near metal nanoparticles can be enhanced by plasmon resonances as well as sharp edges. The enhanced electric field near metal nanoparticles and sharp tips (such as silicon atomic force microscope probes) is confined to a region whose volume is a small fraction of the cube of the incident illumination wavelength. This has the effect of confining the excitation to provide higher spatial resolution and/or more efficient excitation of a nanoscale region. These effects can be used for a variety of applications like guiding electromagnetic energy in subwavelength-sized optoelectronic devices,[1] enhanced fluorescence spectroscopy,[2] Raman spectroscopy,[3,4] near-field imaging,[5] and biosensing.[6] Aperture based scanning near-field optical microscopes (SNOMs)[7–9] that use a subwavelength aperture to confine light below diffraction limit can provide optical resolution in the range of 50–100 nm but are severely limited by poor light transmission efficiency. Apertureless SNOMs[10–12] that use sharp tips for optical imaging have a demonstrated optical resolution of ~15 nm but suffer from poor optical throughput in addition to the problem of separating the large background light from the near field spot. The use of metal nanoparticles as near-field imaging devices potentially combines the high optical resolution associated with apertureless SNOM with excellent light transmission efficiency.

Genov *et al.*[13] studied gold nanodisks separated by small gaps and predicted near field intensity ($|E|^2$) enhancements greater than 10^3. Hao *et al.*[14] theoretically considered metallic nanostructures of different shapes and sizes, including two triangular nanoprisms facing each other tip-to-tip and separated by 2 nm, using the discrete dipole approximation method. They predicted intensity enhancement factors as high as $\sim 5 \times 10^4$. Rechberger *et al.*[15] and Su *et al.*[16] experimentally studied coupling effects between gold nanodisks in an array and for single nanoparticle pairs, respectively. They showed that the resonant wavelength depended on the spacing between particles. Jackson *et al.*[17] have utilized the plasmon coupling in a metallic nanoshell geometry to produce enhancements of Raman scattering. Crozier *et al.*[18] studied antennas of various shapes at midinfrared wavelengths and explored the reasons for electric field enhancement by computing the current distribution in the antennas. They found good agreement between the experimental extinction efficiency and resonant wavelength values with those obtained from finite-difference time-domain (FDTD) computations.

Grober *et al.*[19] showed that the field is enhanced in the gap between triangles in a bowtie antenna in the microwave regime and suggested the possibility of extending this principle to visible wavelengths. In recent work, we have fabricated and experimentally characterized metallic Au bowtie structures with size small enough to resonate at visible wavelengths.[20,21] In this study we extend the microwave[19] and mid-infrared[18] studies of metallic bowties to the critically important optical regime, where triangle dimensions <100 nm. We present detailed finite-difference time-domain (FDTD) electromagnetic computations of field enhancement, resonant wavelength and local current distribution for bowtie antennas with different gap widths. The bowtie antennas we simulate closely mimic the structures that have actually been fabricated and measured experimentally. Our calculations confirm that very high optical intensity enhancements can be obtained for realistic, lithographically fabricated bowtie structures composed of gold, an adhesion layer, indium-tin-oxide layer, and substrate. Obtaining high intensity enhancements from nanostructures that can be reproducibly fabricated represents an important step forward in deploying them for the wide range of applications mentioned above. We find excellent agreement between the resonant wavelength values derived from the FDTD computations and the experimental resonant wavelength values derived from the scattering spectra obtained for individual bowtie antennas. Similar good agreement is found for the predicted peak optical intensity enhancements and measured values.[21] We present a physical

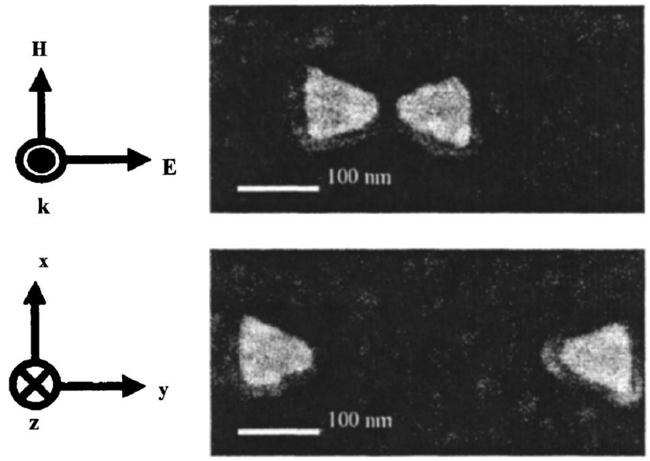

FIG. 1. SEM images of two representative gold bowties on the fused silica-ITO substrate. The polarization of the incident beam and the coordinate system are shown. The simulated structures closely matched the fabricated bowties. The gap width for the bowtie on top is 16 nm.

model for the shift in the resonant wavelength with gap width based on the current distributions in the bowtie antenna and the capacitance of the air gap. Based on the current distribution in the antennas we show a distinct difference between the basis for enhancement at small gap widths (displacement current flowing into the air gap) and larger gap widths (negligible displacement current flowing into the air gap and strong charge confinement at the apex of the triangles in the bowtie antenna).

Figure 1 shows a scanning electron microscopy (SEM) image of the fabricated Au bowties along with the direction of incident beam polarization and the coordinate system. The electric field variation in the vicinity of a bowtie antenna is determined through three-dimensional FDTD electromagnetic simulations,[22] using node sizes of 4 nm along the x, y, and z directions and a total simulation volume of 800 nm (x axis) $\times$ 800 nm (y axis) $\times$ 176 nm (z axis). The bowtie antennas are illuminated from the substrate side by a plane wave polarized along the y direction, and the antennas radiate into free space. The wavelength-dependent dielectric constants used for the bowtie antennas and the substrate are taken from Palik *et al.*[23] and put into a Drude model. Perfectly matched layers (PML) are used at the top and bottom of the simulation domain to completely absorb waves leaving the simulation domain in the direction of propagation. The FDTD simulations assume periodic boundary conditions in the $x-y$ directions, thereby simulating an array of antennas. The interelement spacing between the antennas in the FDTD simulation is chosen to be sufficiently large so that coupling between the antennas has a negligible effect on the near-field distribution in each antenna. This enables a direct comparison between theory and experiment.

All the bowtie antennas simulated have constituent triangles that are equilateral, where each side is 88 nm in length and the radius of curvature at the triangle apex is equal to 12 nm. The gap between the triangles in the bowtie is varied from 16 nm to 500 nm. The thickness of each bowtie antenna simulated is 24 nm (20 nm gold layer +4 nm chrome sticking layer). The substrate is fused silica (refractive index, $n=1.47$) with a 52 nm layer of indium tin oxide (ITO, $n=1.95$) evaporated on it, which has the effect of improving the ability to produce a high-quality e-beam structure at this small size scale. These values are very close to the specifications of the fabricated bowties.[13]

Figure 2(a) shows a color (gray scale) map and a surface plot of the calculated intensity enhancement, 4 nm above a bowtie antenna with a 16 nm gap. These plots are derived from FDTD calculations using a node size of 2 nm, described in more detail below. Figure 2(b) shows the peak near-field intensity ($|E|^2$) enhancement values for bowties with 16 nm and 160 nm gaps as a function of excitation wavelength. The bowtie antenna with a 16 nm gap has a peak near-field intensity enhancement of 1645 relative to the incident beam and is spatially confined to a 20 nm region in the x-y direction, measured as a full width at half-maximum (FWHM) value. The maximum intensity value is found to be close to each triangle apex, 4 nm above the bowtie surface. The direction of the maximum field for gaps smaller than 60 nm is along the plane of the bowties in the y direction, and for gaps greater than 60 nm is in the direction of propagation (z direction), perpendicular to the surface of the metal. These calculated values are in good agreement with local intensity enhancements in the metal obtained by two-photon excited photoluminescence studies reported earlier.[21] We now describe the FDTD simulations themselves in order to extract a deeper understanding of the physical processes involved in these large enhancements.

A full description of our bowtie fabrication process and the total internal reflection (TIR) experimental setup to obtain scattering spectra from individual bowties is given elsewhere.[20] In order to compare the simulated spectra obtained from the FDTD computations with the experimental data, we compute the far-field scattering efficiency[24] of the bowtie antennas at different wavelengths. In the experiment, using TIR with s-polarized light, there is no transmitted wave when the bowtie antenna is not present, while a scattered wave radiating into the far field is produced in the presence of the antenna. In the FDTD calculation for triangles much smaller in extent than a wavelength, we calculate the scattering efficiency (Q_{scat}) as the ratio of scattering cross section (C_{scat}) to the metal antenna area (A). We compute the current density distribution in the antennas and use this to compute far-field radiated power (W_{rad} in watts), thereby obtaining the scattering cross section (C_{scat}) which is defined by the relation

$$C_{\mathrm{scat}} = W_{\mathrm{rad}}/I, \tag{1}$$

where $I=E^2/2\eta$ is the calculated incident power density ($\mathrm{W}/\mu\mathrm{m}^2$) on an antenna with a known current distribution, E is the incident electric field on the antenna, and η is the impedance of the medium containing the incident wave.

The displacement current density, $\mathbf{J_D}=j\omega\varepsilon_0\mathbf{E}$, in the x-y plane in the gap normal to the edge of the metal is continuous with the current density $\mathbf{J_m}$ normal to the edge inside the metal. Consequently, the enhanced field in the gap is due to the enhanced current density near the tips of the constituent triangles of the bowtie. To calculate C_{scat}, the total current in

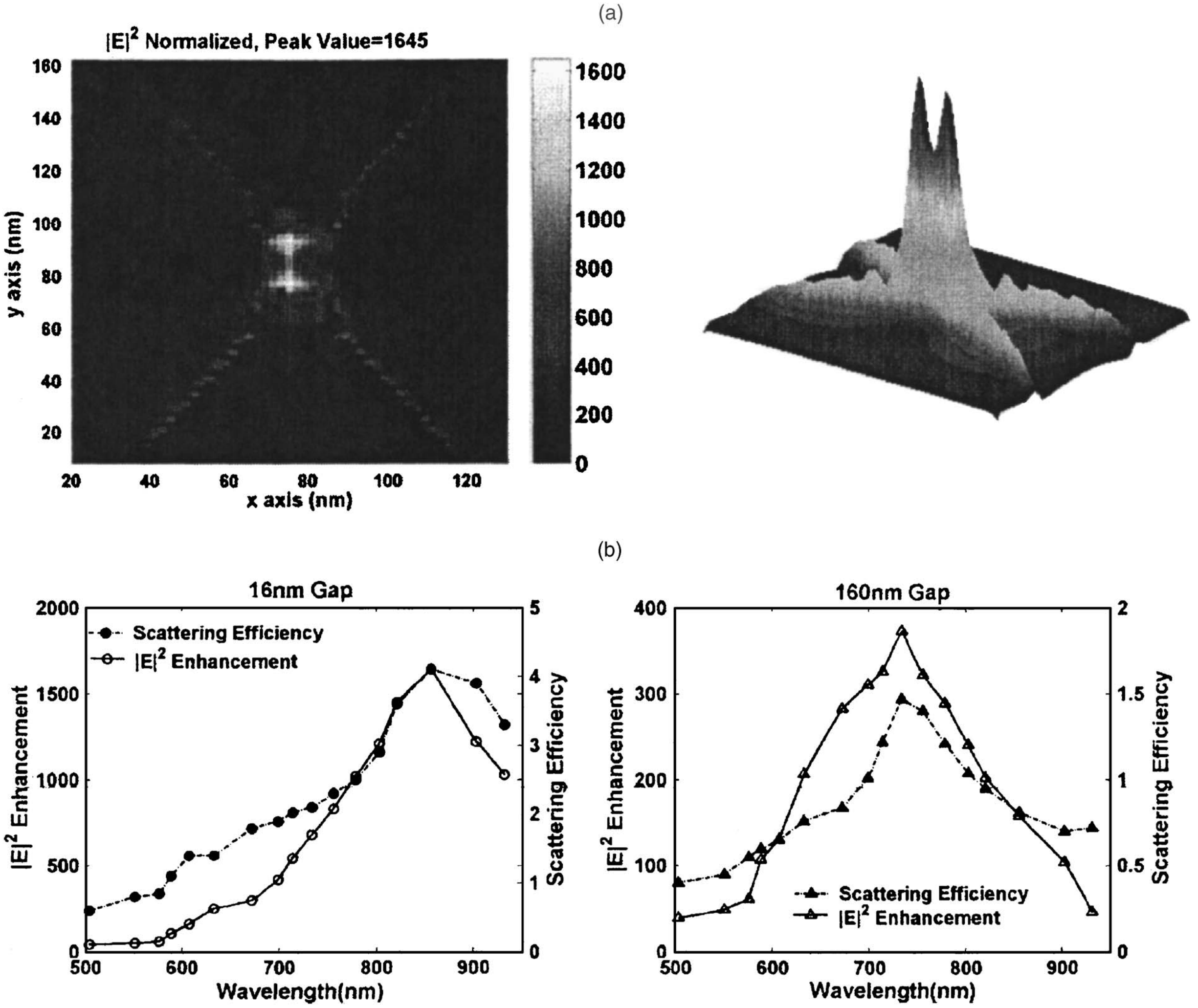

FIG. 2. (a) Left, FDTD calculated $|E|^2$ enhancement at the top surface of a 16 nm gap bowtie antenna, where the two triangles are at the top and bottom of the figure. Right, a 3D surface plot of the peak intensity variation across the bowtie is also shown, with a different color scale and with the triangles at the right and left of the image. The peak value of intensity in both plots is 1645. The illumination is from the substrate side, the illumination wavelength is 856 nm, and a node size of 2 nm was used for these images. (b) $|E|^2$ enhancement vs wavelength and scattering efficiency (Q_{scat}) vs wavelength from FDTD simulations for two different gaps. The peak enhancement and scattering efficiency for a bowtie for the 16 nm gap width case is 1645 and 4.1, respectively.

the y direction in the metal of the antenna is obtained by integrating the polarization current density (J_{ym}) over x and z

$$\mathbf{J}_m = j\omega(\varepsilon_r - 1)\varepsilon_0\mathbf{E}, \tag{2}$$

$$(n + jk)^2 = \varepsilon_r, \tag{3}$$

where $\mathbf{E}$ is the electric field obtained from the (near-field) FDTD simulation, ω is the angular frequency, ε_0 is the permittivity of free space, ε_r is the relative complex permittivity of the metal and $(n+jk)$ is the complex, wavelength-dependent refractive index taken from Palik *et al.*[23]

The current density in the antenna is largest at resonance. Ramo *et al.*[25] provide a systematic method to compute average radiated power (in watts) from an antenna, which has a known current distribution. Figure 2(b) shows the calculated variation in scattering efficiency with wavelength for bowtie antennas with two different gaps. To make a fair comparison with the experimental data, the radiated power obtained from the FDTD simulations is multiplied by a constant factor to model the finite acceptance angle of the collection lens (0.8 NA) used in the experiment. The theoretical scattering efficiency at resonance is highest for the smallest gaps (Q_{ext}=4.1 for a 16 nm gap) indicating that the antennas with smaller gap radiate more power relative to their area. A comparison of the resonant wavelength value obtained from the scattering efficiency curves and the scattering spectra obtained from experiment is shown in Figs. 3(a)–3(c). All the experimental photon counts were scaled to match the peak theoretical FDTD calculated scattered power for a 232 nm gap in Figs. 3(a)–3(c). Figure 3(d) shows the peak scattering (resonant) wavelength as a function of gap length for both theory and experiment. We find excellent agreement between experiment and theory for the peak wavelengths. The absolute experimental scattering cross section could not be accurately computed because it was not possible to determine the

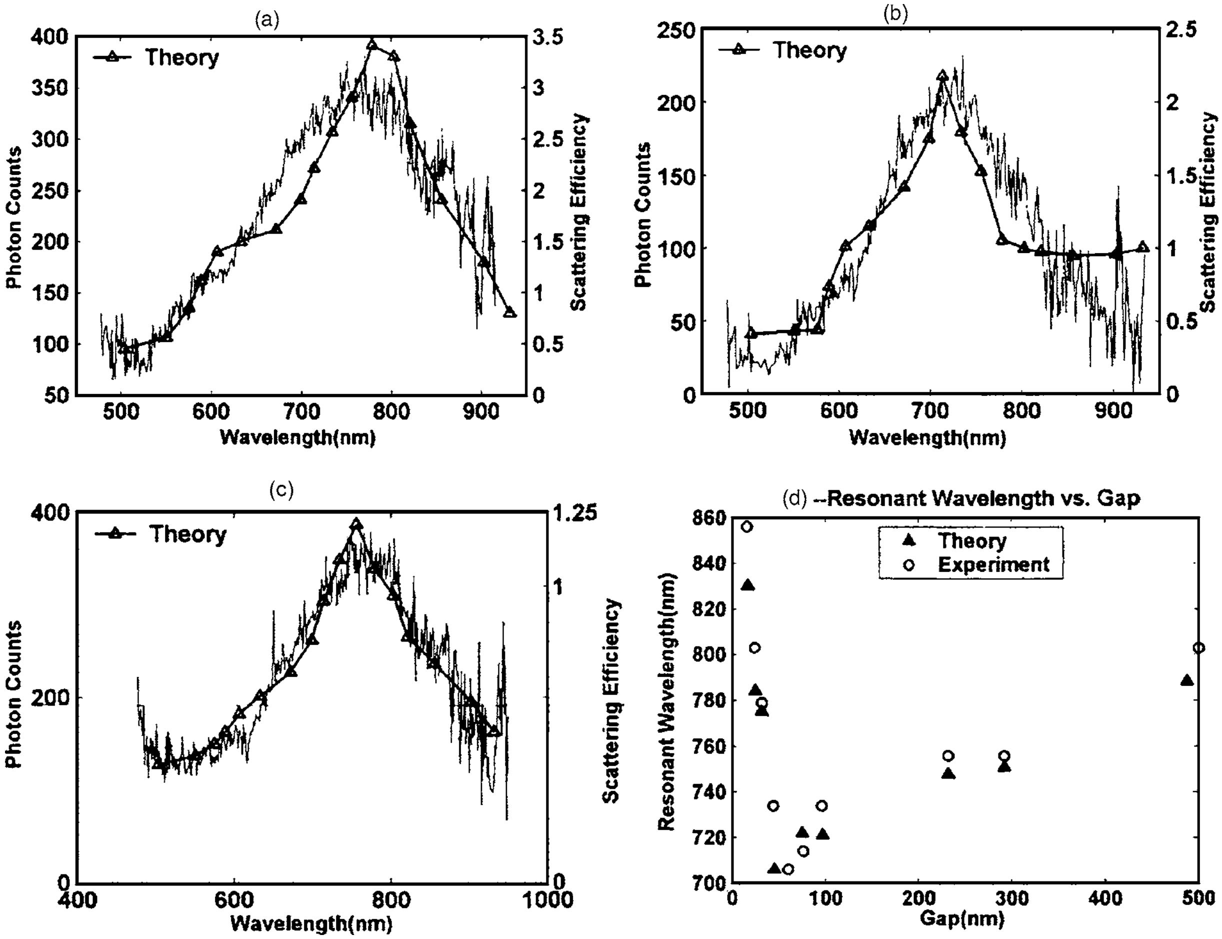

FIG. 3. The plots (a)–(c) show a comparison of the spectra obtained from FDTD calculations (line with triangles) and experiments (curve with experimental noise) for different gap sizes. λ_{rT} and λ_{rE} are the theoretical and experimental resonant wavelengths. (a) gap=32 nm, $\lambda_{rT}=779$ nm, $\lambda_{rE}\sim 776$ nm; (b) gap=60 nm, $\lambda_{rT}=706$ nm, $\lambda_{rE}\sim 720$ nm; (c) gap=232 nm, $\lambda_{rT}=756$ nm, $\lambda_{rE}\sim 748$ nm. (d) shows the variation in resonant length with gap for FDTD calculations (closed triangles) and experimental measurements (open circles).

equivalent incident power on the bowtie with TIR excitation as described in Ref. 20. The experimental scattering spectra shown here rest on the assumption that as a function of wavelength, the incident power is proportional to the measured illumination power from the source scaled by the detection efficiency of our microscope, whose calibration is detailed in Ref. 20.

At resonance the bowtie with the smallest gap has the largest peak current density and the peak current density increases as the gap width decreases. The calculated instantaneous vector surface current densities in bowties with 16 nm and 500 nm gap widths, respectively, for an incident *E*-field excitation of 1 V/m, are shown in Fig. 4. We observe that the current vectors are predominantly in the *y* direction as this is the polarization of incident illumination. However, there is a critical difference in the magnitude and position of peak current density for 16 nm and 500 nm gap widths. For a bowtie with 16 nm gap width, shown in Fig. 4(a), the peak current density lies at the apex of the triangle and the current density is fairly uniform with *x* across the tip region. The peak current density is confined to a small fraction of the total bowtie area. There is a strong displacement current flowing in the air gap between the triangles and it is continuous with the conduction current as mentioned above. For a 16 nm gap, the resonance is at 856 nm wavelength, where the real part of the dielectric constant of the metal is negative and hence the impedance of the metal is inductive. Consequently, we might expect to observe a plasmon resonance of the coupled structure controlled by the capacity of the gap and the inductance of the tip region rather than by the dimensions of the relatively large triangles. This is true for gaps smaller than 60 nm, where the antenna resonance is dominated by the capacitance of the air gap with its associated field in the *y* direction. In this regime, the resonant wavelength decreases with increasing gap (decreasing capacity). Similar calculations were made for 20 nm wide gold rods separated by 16 nm gaps. The resonant frequencies for gaps less than 32 nm were almost identical to those for the equilateral triangles, thus indicating that with small gaps, the resonance is controlled by the large gap capacity.

For gaps larger than 60 nm, the displacement current tends to flow into a region further from the tip than it would for small gaps. Since the capacity of the air gap is small, the total current flowing into the gap is small and the conduction current density is parallel to and peaked along the edges of the triangle at the metal and/or air interface as shown in Fig.

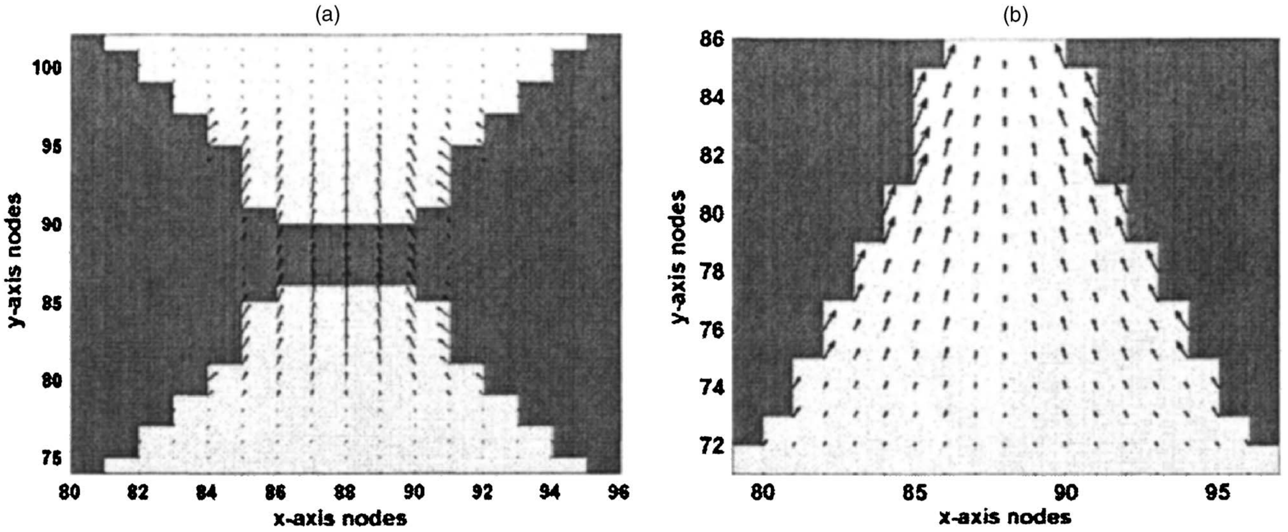

FIG. 4. Vector plot of the instantaneous surface current for two gap widths. (a) 16 nm gap width bowtie, instantaneous peak current density in the metal=0.1218 μA/μm, and instantaneous peak displacement current density=0.1321 μA/μm. (b) One triangle in the 500 nm gap width bowtie is shown, instantaneous peak current density=0.0558 μA/μm. The node size used in the simulation is 4 nm. The incident field, *E*, on the bowtie is 1 V/m. The current is negligible in the portions of the bowtie not shown in the figure. For the 16 nm gap width case the current is peaked at the apex of the triangle and is strongly confined. For the 500 nm gap width, the current is peaked at the triangle edges and is parallel to the metal and/or air interface.

4(b). In this regime, the *E*-field outside the metal and hence the displacement current is maximum in the *z* direction normal to the plane of the triangles, the coupling between the triangles is decreased and the current distribution approaches that of a single triangle.

Figures 5 and 6 show, respectively, the total current and peak current density along long axis of the bowtie for different gap widths. For gaps less than 60 nm, the magnitude of the total current (Fig. 5) and peak current density (Fig. 6) are largest at the apex of the triangle. For gaps greater than or equal to 60 nm, the position of the peak current density moves into the triangle (Fig. 6). A gap width of 60 nm coincides with the theoretical and experimental resonance wavelength inflection point, as shown in Fig. 3(d). As the gap width increases beyond 60 nm, the peak field and displacement current near the tip is normal to the plane of the triangle and tends to terminate further and further back on the triangle from which it leaves, similar to the behavior seen in the mid-IR.[18] In this case the displacement current flows back to the same triangle rather than to the other triangle, and so the effective self-capacity slowly increases causing the resonant wavelength to increase as the triangles become

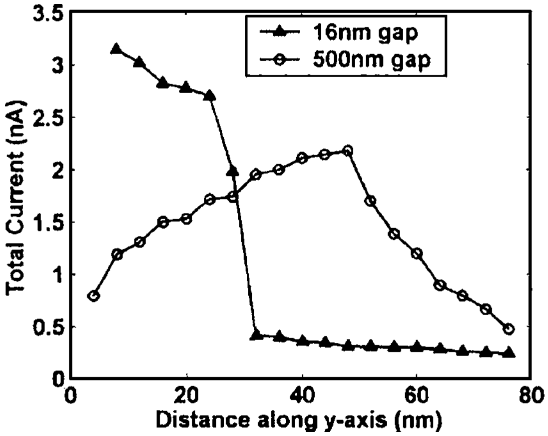

FIG. 5. Plot of total current in one triangle of the bowtie vs the distance along the bowtie from the apex (0 nm on the abscissa) to the base. The total current is highest at the apex for the 16 nm gap bowtie and the peak total current lies within the triangle for the case of a 500 nm gap bowtie.

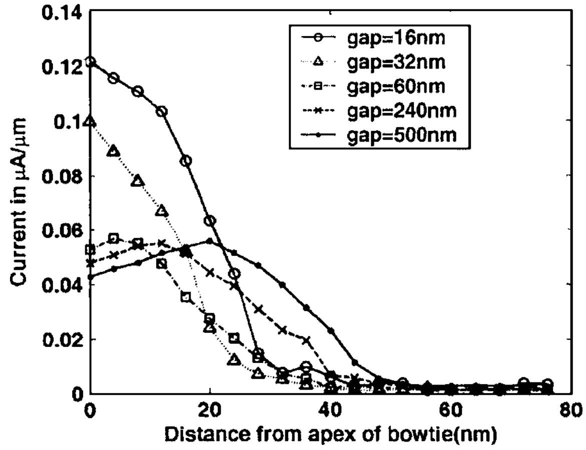

FIG. 6. Peak current density variation as a function of distance from the apex of one triangle of the bowtie. Zero on the *x*-axis refers to the apex of the bowtie. The abscissa values indicate increasing distance into the triangle along a perpendicular line from the apex to the base of the triangle. The peak current (I_p) and position of peak current density (y_p) for different gap widths is as follows: (i) gap=16 nm, I_p=0.1218 μA/μm, y_p=0 nm; (ii) gap=32 nm, I_p=0.0993 μA/μm, y_p=0 nm; (iii) gap=60 nm, I_p=0.0566 μA/μm, y_p=4 nm; (iv) gap=240 nm, I_p=0.0550 μA/μm, y_p=12 nm; (v) gap=500 nm, I_p=0.0552 μA/μm, y_p=20 nm.

uncoupled. As the gap width increases, the gap capacitance becomes negligible and hence the current maximum lies within the triangle. The charge density and associated field in the z direction are high (but not necessarily a maximum) at the apex.

We note that the difference between a bowtie and any other pair of metallic structures separated by a gap would also manifest itself in the magnitude and pattern of current density distribution. A qualitatively similar behavior with regard to the shift in resonance wavelength would still be observed, but the inflection point and the peak field enhancement close to the gap would be different. This electromagnetic picture of the coupled system is a complementary alternative to an interpretation of the behavior based on a coupled-dipole approximate calculation by Hao *et al.*[14]

In conclusion, we have studied metallic bowtie antennas with ~75 nm dimensions as a function of gap by FDTD computations, in order to compare with optical measurements and extract values of enhancements and a picture of the currents in the antenna. The resonant wavelengths obtained from theory and experiment were in excellent agreement, as were the maximum intensity enhancements. A simple capacitive-inductive model based on current distribution in the antennas was used to interpret the variation in resonant wavelength and enhancement. By fabricating an antenna of this type on a near-field probe, enhanced optical spectroscopy and imaging well below the diffraction limit will be possible.

This work was supported in part by the U. S. Department of Energy Grant No. DE-FG03-00ER45815 (G.K.) and by the National Institutes of Health Grant No. GM65331-R21 (W.E.M.). The authors wish to thank Professor Andy Neureuther, University of California, Berkeley for use of TEMPEST 6.0 FDTD software developed by his group.

---

*Electronic address: arvisun@stanford.edu

†Currently with the Division of Engineering and Applied Sciences, Harvard University.

[1] S. A. Maier, P. G. Kik, and H. A. Atwater, Appl. Phys. Lett. **81**, 1714 (2002).

[2] H. F. Hamann, M. Kuno, A. Gallagher, and D. J. Nesbitt, J. Chem. Phys. **114**, 8596 (2001).

[3] A. Hartschuh, E. J. Sanchez, X. S. Xie, and L. Novotny, Phys. Rev. Lett. **90**, 095503-1 (2003).

[4] M. Moskovits, Rev. Mod. Phys. **57**, 783 (1986).

[5] S. Takahasi and A. V. Zayats, Appl. Phys. Lett. **80**, 3479 (2002).

[6] Y. Cao, R. Jin, and C. A. Mirkin, Science **297**, 1536 (2002).

[7] H. Bethe, Phys. Rev. **66**, 163 (1944).

[8] E. Betzig and R. J. Chichester, Science **262**, 1422 (1993).

[9] B. Hecht, B. Sick, U. P. Wild, V. Deckert, R. Zenobi, O. J. F. Martin, and D. W. Pohl, J. Chem. Phys. **112**, 7761 (2000).

[10] S. Kawata and Y. Inouye, Ultramicroscopy **57**, 313 (1995).

[11] F. Zenhausern, Y. Martin, and H. K. Wickramasinghe, Science **269**, 1083 (1995).

[12] R. Hillenbrand and F. Keilmann, Appl. Phys. Lett. **80**, 25 (2002).

[13] D. A. Genov, A. K. Sarychev, V. M. Shalaev, and A. Wei, Nano Lett. **4**, 0343710 (2004).

[14] E. Hao and G. C. Schatz, J. Chem. Phys. **120**, 357 (2004).

[15] W. Rechberger, A. Hohenau, A. Leitner, J. R. Krenn, B. Lamprecht, and F. R. Aussenegg, Opt. Commun. **220**, 137 (2003).

[16] K. H. Su, Q. H. Wei, X. Zhang, J. J. Mock, D. R. Smith, and S. Schultz, Nano Lett. **3**, 1087 (2002).

[17] J. B. Jackson, S. L. Westcott, L. R. Hirsch, J. L. West, and N. J. Hallas, Appl. Phys. Lett. **82**, 257 (2003).

[18] K. B. Crozier, A. Sundaramurthy, G. S. Kino, and C. F. Quate, J. Appl. Phys. **94**, 4632 (2003).

[19] R. D. Grober, R. J. Schoelkopf, and D. E. Prober, Appl. Phys. Lett. **70**, 1354 (1997).

[20] D. P. Fromm, A. Sundaramurthy, P. J. Schuck, G. S. Kino, and W. E. Moerner, Nano Lett. **4**, 957 (2004).

[21] P. J. Schuck, D. P. Fromm, A. Sundaramurthy, G. S. Kino, and W. E. Moerner, Phys. Rev. Lett. **94**, 017402 (2005).

[22] TEMPEST 6.0, Electronics Research Laboratory, University of California, Berkeley, California.

[23] E. D. Palik, *Handbook of Optical Constants* (Academic, Orlando, FL, 1985).

[24] C. F. Bohren and D. R. Huffman, *Absorption and Scattering of Light by Small Particles* (Wiley, New York, 1998).

[25] S. Ramo, J. R. Whinnery, and T. Van Duzer, *Fields and Waves in Communication Electronics*, 2nd ed. (Wiley, New York, 1984), pp. 586–589.